Corrected Proof

Interaction of a dam-break wave with an obstacle over an erodible floodplain

Cristiana Di Cristo, Massimo Greco, Michele Iervolino and Andrea Vacca

ABSTRACT

Because of climate change, flood-prone areas are more and more frequently exposed to potential casualties and damage. The capability of the flow to carry relevant quantities of sediments during these critical events adds to the further complexity of the resulting scenarios. The interaction between the flow and the obstacles in flood-inundated areas contributes to an increase in the hazard level and constitutes a relevant concern in the framework of risk analysis. Despite this relevance, the existing literature on the topic is relatively scarce, especially for the estimation of the forces acting on rigid obstacles in the presence of a mobile bed. In the present paper, a recent two-phase shallow-water morphodynamical model, particularly suited for the analysis of fast geomorphic transients, is applied for the numerical simulation of the propagation of a dam-break wave over an erodible floodplain in the presence of a rigid obstacle. The geometry of the test-case is inspired by a recent fixed-bed study reported in the literature, for which extensive experimental and numerical data concerning the flow field and the dynamic loading against the obstacle are available. Results of the numerical simulations contribute to highlight the effects of the obstacle on the changes in the bottom topography.

Key words | dam break, impact force, mobile bed, two-phase model

Cristiana Di Cristo
Massimo Greco
Andrea Vacca
Università di Napoli 'Federico II',
via Claudio 21, Napoli 80125,
Italy

Michele Iervolino (corresponding author)
Università della Campania 'Luigi Vanvitelli',
via Roma 9, Aversa (CE) 81031,
Italy
E-mail: *michele.iervolino@unicampania.it*

INTRODUCTION

The presence of obstacles, such as bridge piers, is common in rivers and channels, but they may also be encountered in potentially flooded areas. The magnitude of floods caused by intense rainfall is becoming more and more severe owing to climate change (Hoerling *et al.* 2001). In turn, the exposition of initially dry areas to flood waves arising from the failure of embankments or dikes has increased. In these cases, the wave impacts on a variety of obstacles such as buildings, piles, industrial and commercial structures, with damaging consequences. The presence of structures in flooding areas has many aspects that require adequate investigation, especially in case of a severe flood like that following a dam break. First, an appropriate risk control strategy, essential to prevent damage and to reduce the losses, requires the individuation of risk areas and the selection of adequate measures for its mitigation, such as structural countermeasures including longitudinal walls, deflection and redirecting structures (Hung *et al.* 1984). Second, obstacles may considerably affect the flood wave propagation, especially when they are close to the dam and in the first moments after the break (Soares-Frazão & Zech 2007). Third, the impacting force on the obstacles may produce structural damage even compromising their stability.

Finally, the capability of the flood to carry relevant quantities of sediment in the flow is another important aspect. In this case, the sediment concentration influences the characteristic of the mixture flow, moving from the bed and suspended load to debris transport. The interaction between the liquid–solid mixture and the presence of obstacles in the inundated areas both contribute to affect the flood wave propagation. On the one hand, the obstacles

doi: 10.2166/hydro.2019.014

Downloaded from https://iwaponline.com/jh/article-pdf/doi/10.2166/hydro.2019.014/569419/jh2019014.pdf
by guest

Corrected Proof

deviate the flow pattern, and, on the other hand, the morphological change induced by the flow may expose the obstacle to unexpected loading condition, therefore contributing to its structural damage. For these reasons, the propagation of flood waves over loose sediment bed and its interaction with obstacles constitute a relevant concern in the framework of risk analysis.

In conclusion, the study of the complex interaction between the flood wave and the obstacles is extremely important to evaluate the hazard levels and to support the design of structural countermeasures. This requires the knowledge of both the hydro- and sediment dynamics and the force acting on the structure by the flow (Thieken *et al.* 2005).

The dynamic impact of a flood wave on a structure and the consequent damage is, in some cases, evaluated by empirical formulas or adopting simplified analysis (e.g. Kelman & Spence 2004). However, these approaches may produce incorrect indications since they are usually derived through site-specific studies. Alternatively, the principal kinematics characteristics of the dynamic impact and the acting force may be numerically reproduced.

The study of a wave impacting on an obstacle has been widely investigated both experimentally and numerically considering clear water flowing on non-erodible beds (e.g. Bukreev 2009; Chen *et al.* 2014); debris flows (e.g. Canelli *et al.* 2012; Scheidl *et al.* 2013), and snow and dry avalanches (e.g. Tai *et al.* 2001; Chiou *et al.* 2005; Teufelsbauer *et al.* 2009; Cui & Gray 2013; Faug 2015).

Among the numerical studies concerning debris flows, Kattel *et al.* (2018) modelled debris impacting tetrahedral obstacles of different dimensions, number and orientation, reproducing the behaviour of the liquid–solid mixture with the quasi-three-dimensional two-phase model of Pudasaini (2012). The presence of obstacles may increase the solid- and fluid-phase separation, and it strongly influences the wave propagation. Debris flow propagation in urban areas has been recently simulated by Gao *et al.* (2017) with a depth-integrated continuum model, demonstrating that the obstacles increase the depth and the velocity of the flow and the impact pressure. More recently, Di Cristo *et al.* (2019) reproduced the impact force of a mud flow on a rigid obstacle with both a single-phase, shear-thinning power-law model and a two-phase model, which separately considers the liquid and solid phases. The comparison suggests that in the situations where the liquid and solid phases remain mixed, the essential features of the interaction with the obstacles and the maximum impact force are similarly predicted by the two models, while some differences are registered in the cases characterized by phase separation.

Concerning clear water flows over non-erodible beds, among the different experimental studies, only few evaluated the impact force. Lobovsky *et al.* (2014) performed laboratory tests measuring the load produced from a dam break on a vertical wall using miniaturized pressure sensors, while Aureli *et al.* (2015) evaluated the impact force on a single rigid obstacle.

With regard to numerical studies, Wang *et al.* (2000) used Saint Venant Equations with a second-order total variation diminishing finite-difference method for solving 1D and 2D dam-break in the presence of obstacles, also discussed the effect of bed slope, bottom friction and the tailwater/reservoir depth ratio. Successively, many other works considered the shallow-water formulation as a reasonable approach for the simulation of these complex processes. For example, Shige-eda & Akiyama (2003) investigated two-dimensional (2D) flood flows and the hydrodynamic force acting on structures, showing that the prediction accuracy of the shallow-water model is reasonable for both hydrodynamics and force on structures. Bukreev (2009) successfully applied a shallow-water model to predict the dynamic action exerted by a dam-break wave on a vertical wall. Soares-Frazao & Zech (2008) and El Kadi Abderrezzak *et al.* (2009) investigated the potentiality of a depth-averaged shallow-water model in reproducing the propagation in urban areas of both flash floods and dam-break waves. Numerical results, in terms of both flow depths and velocities, fairly agree with experimental ones, although some discrepancies were observed around buildings, where the flow is strongly 3D. More recently, Aureli *et al.* (2015) compared the predictions of a 2D depth-averaged model, a 3D Eulerian two-phase model and a 3D smoothed particle hydrodynamics model, in the simulation of the forces exerted by a dam-break wave on a rigid squat structure. Comparing the numerical and the experimental results, the authors found that the error in the peak load for the

Downloaded from https://iwaponline.com/jh/article-pdf/doi/10.2166/hydro.2019.014/569419/jh2019014.pdf
by guest

Corrected Proof

2D model based on the shallow-water approach was in the order of 10%.

As far as the simultaneous presence of obstacles and of an erodible floodplain are concerned, from the experimental point of view, the tests by Palumbo *et al.* (2008) and the test-cases studied under the NSF-Pire project (Soares-Frazão *et al.* 2012), regarding a dam-break in an erodible channel with a sudden enlargement, contributed to shed some light on the basic elements of the interaction of the flood wave with rigid walls. However, they neither considered any obstacle in the floodplain nor evaluated the impact forces.

The numerical analyses which were subsequently developed, support the idea that for these kinds of processes, the shallow water approximation represents a suitable framework, provided that adequate modelling of the non-equilibrium sediment transport is accounted for. To match this latter requirement, several non-equilibrium models have been proposed, which can be grouped into mixture single layer (e.g. Wu & Wang 2007), multi-layer (e.g. Capart & Young 2002; Savary & Zech 2007; Li *et al.* 2013; Swartenbroekx *et al.* 2013) or multi-phase (e.g. Dewals *et al.* 2011; Greco *et al.* 2012; Rosatti & Begnudelli 2013; Di Cristo *et al.* 2016).

The objective of this paper is to numerically analyse the propagation of a dam-break wave over an erodible floodplain in the presence of a rigid obstacle. The results of both fixed and erodible bed conditions are compared for understanding the role of the sediment mobility on the hydrodynamics and the impact force. The shallow-water two-phase model of Di Cristo *et al.* (2016) is adopted for reproducing the impact of a dam break considering the same geometry of the fixed-bed test case by Aureli *et al.* (2015). In this study, both fixed bed and mobile bed conditions are reproduced, and in the latter case, two different tests characterized by two different sediments constituting the loose bed are considered. The preliminary study of Di Cristo *et al.* (2018a) shows a comparison between the fixed and mobile bed tests. In the present paper, the comparison is completed with the results presented in terms of the temporal evolution of the flow field, the bottom deformation and the impact force on the obstacle.

The article is organized as follows. In the 'Material and Methods' section, both the test-case and the morphodynamical model adopted for the numerical simulations are described. Some details concerning the numerical solution method are also given. In the section 'The Considered Test-Case', results of the numerical simulations are presented and discussed. Finally, the main conclusions are drawn.

MATERIAL AND METHODS

The geometry of the test-case considered for the numerical simulations has been selected from the existing literature on clear water dam-break waves impacting against rigid obstacles over a fixed bed. Namely, the study carried out by Aureli *et al.* (2015) has been considered. In what follows, both the test-case and the morphodynamical model adopted for the numerical simulations are described.

THE CONSIDERED TEST-CASE

Figure 1 reproduces the plan view of the test-case by Aureli *et al.* (2015). The flow is caused by the sudden removal of the gate, which triggers the propagation of a dam-break wave over the downstream floodable area.

In the numerical simulations, the floodplain can be assumed as non-erodible or constituted by loose sediment, namely uniformly graded sand. In the former case, the resulting layout exactly coincides with the scheme investigated by Aureli *et al.* (2015), while in the latter case two scenarios have been considered by changing the sediment diameter.

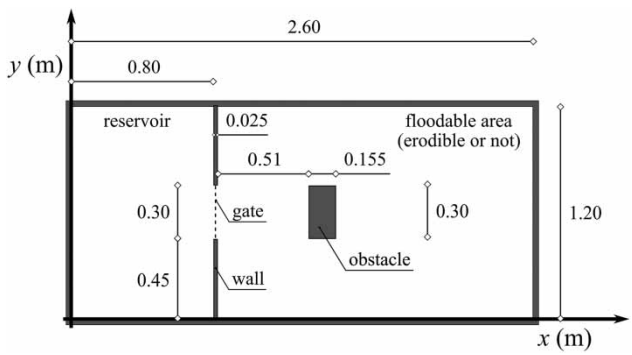

Figure 1 | Sketch of the considered test-case (dimensions are in metres).

Downloaded from https://iwaponline.com/jh/article-pdf/doi/10.2166/hydro.2019.014/569419/jh2019014.pdf
by guest

Corrected Proof

THE MATHEMATICAL MODEL

A brief description of the model presented in Di Cristo *et al.* (2016) is provided below, whereas the reader is referred to the original reference for further details about the underlying assumptions and the subsequent limitations, along with a more exhaustive description of the numerical method employed for the simulation. Since in the present application the suspended load has been neglected, the mathematical model is constituted of the equations expressing the mass and momentum conservation for the liquid (Equations (1) and (3)) and the solid phase transported as bedload (Equations (2) and (4)). Finally, Equation (5) describes the evolution of the loose bed. They read as follows:

$$\frac{\partial \delta_l}{\partial t} + \nabla \cdot (\delta_l \mathbf{U}_l) - p e_B = 0 \tag{1}$$

$$\frac{\partial \delta_s}{\partial t} + \nabla \cdot (\delta_s \mathbf{U}_s) - (1-p) e_B = 0 \tag{2}$$

$$\frac{\partial \delta_l \mathbf{U}_l}{\partial t} + \nabla \cdot (\delta_l \mathbf{U}_l \mathbf{U}_l) + \nabla \left(\frac{g h^2}{2} \right) + g h \nabla (z_B) + \mathbf{S}_l = 0 \tag{3}$$

$$\frac{\partial \delta_s \mathbf{U}_s}{\partial t} + \nabla \cdot (\delta_s \mathbf{U}_s \mathbf{U}_s) + \frac{r}{r+1} \nabla \left(\frac{g \delta_s^2}{2 C_s} \right) + g \delta_s \frac{r}{r+1} \nabla (z_B) + \mathbf{S}_s = 0 \tag{4}$$

$$\frac{\partial z_B}{\partial t} + e_B = 0 \tag{5}$$

in which t is the time, g denotes the gravity acceleration, $r = (\rho_s - \rho_l)/\rho_l$ with ρ_l and ρ_s are constant liquid and solid densities, respectively. As far as the flow variables are concerned, δ_l denotes the liquid-phase volume for the unit bottom surface and δ_s is the solid-phase volume transported as bedload for the unit bottom surface. Hence, the free surface and bottom elevation are denoted by z_w and z_B, respectively, $h = z_w - z_B = \delta_l + \delta_s$. $\mathbf{U}$ is the phase-averaged velocity vector, with the subscript l and s used to denote the water and the solid phase, respectively. For both phases, the second-order tensor $\mathbf{UU}$ denotes the diadic product of the phase-averaged velocity with itself. C_s is the bedload volume concentration and e_B is the bottom erosion/deposition rate.

The source terms of momentum equations $\mathbf{S}_l$ and $\mathbf{S}_s$ are given by the following formulas:

$$\mathbf{S}_l = \frac{\mathbf{U}_l}{C_{Ch}^2} |\mathbf{U}_l| - (r+1) \mu_d g \delta_s \frac{r}{r+1} \frac{\mathbf{U}_s}{|\mathbf{U}_s|} - \alpha (r+1) \mathbf{U}_s |\mathbf{U}_s| + g \delta_s s_B + \frac{\mathbf{D}}{\rho_l} \tag{6}$$

$$\mathbf{S}_s = \mu_d g \delta_s \frac{r}{r+1} \frac{\mathbf{U}_s}{|\mathbf{U}_s|} + \alpha \mathbf{U}_s |\mathbf{U}_s| - \frac{\mathbf{D}}{\rho_l} \tag{7}$$

where μ_d is the dynamic friction coefficient, C_{Ch} denotes the dimensionless Chezy coefficient, s_B is the bottom slope, $\mathbf{D}$ is the drag force of the liquid on the solid particle and α is the coefficient needed to evaluate the collisional stresses. In Equation (7), the first two terms represent the ratio $\tau_{B,s}/\rho_s$, where the bottom shear stress, $\tau_{B,s}$ accounts for both frictional and interparticle collisional stresses. In Equation (6), the first four terms represent the ratio $\tau_{B,l}/\rho_l$, where the bottom shear stress on the liquid phase, $\tau_{B,l}$, is expressed as the difference between the shear stress which would act upon the bottom in the absence of sediment transport and the momentum transferred to the solid phase $\tau_{B,s}$. The drag force $\mathbf{D}$ is evaluated as follows:

$$\mathbf{D} = \rho_l C_D \frac{\delta_s}{d} (\mathbf{U}_l - \mathbf{U}_s) |\mathbf{U}_l - \mathbf{U}_s| \tag{8}$$

where C_D is a bulk drag coefficient and d is the sediment particle diameter. The bottom entrainment/deposition is evaluated by means of the following formula (Pontillo *et al.* 2010):

$$e_B = w_s \frac{T^{3/2} - C_s}{1-p} \tag{9}$$

in which w_s denotes the sediment settling velocity, corrected to account for its dependence on C_s through the well-known semi-empirical formula by Richardson & Zaki (1954). The dimensionless mobility parameter T, which accounts for the excess of the mobilizing stresses onto the bottom surface with respect to the resisting ones (Van Rijn 1984), is

Downloaded from https://iwaponline.com/jh/article-pdf/doi/10.2166/hydro.2019.014/569419/jh2019014.pdf
by guest

Corrected Proof

evaluated through the following formula:

$$T = \frac{|\boldsymbol{\tau}_{B,l} + \boldsymbol{\tau}_{B,s} - \boldsymbol{\tau}_c - \boldsymbol{\tau}_B|}{|\boldsymbol{\tau}_c + \boldsymbol{\tau}_B|} \tag{10}$$

where τ_c is the threshold shear stress for particle motion and τ_B is the magnitude of Mohr–Coulomb stress at the bottom, depending on the static friction coefficient μ_s. Even if the coefficients α and C_D could be estimated from the existing empirical formulas, they are evaluated in the model by means of the following relations, deduced to comply with the equilibrium empirical formulas for transport at capacity (Di Cristo *et al.* 2016):

$$\begin{aligned} \alpha &= \frac{(1-c_1) - k_1(\mu_d - s_B)}{(r+1)k_2^2}, \\ C_D &= \frac{1-c_1}{k_1} \frac{\rho_l g dr}{[C_{Ch}\tau_0^{1/2} - k_2(\tau_0 - \tau_c)^{1/2}]^2} \end{aligned} \tag{11}$$

where k_1 and k_2 are the following two dimensionless coefficients:

$$k_1 = \frac{1}{2\mu_s} \frac{2 + (1-p)^{2/3}}{1 + (1-p)^{2/3}} \tag{12}$$

$$k_2 = \frac{K_{MPM}}{k_1} \tag{13}$$

In Equation (13), K_{MPM} is the Meyer–Peter and Müller formula coefficient and c_1 is a dimensionless model parameter. With the above closures, the model application requires the definition of only three independent dimensionless parameters. Two of them, C_{Ch} and K_{MPM}, may be evaluated from the standard literature. The remaining free model parameter c_1 is bounded between the lower and upper limits theoretically deduced, with very little sensitivity of the results to its variation (Di Cristo *et al.* 2016).

The system of Equations (1)–(5) is solved with a numerical code developed by the authors employed also in Di Cristo *et al.* (2016) and Di Cristo *et al.* (2018b). The numerical method, using 2D unstructured quadrilateral meshes, relies on a mixed cell-centred (CCFV) and node-centred finite-volume discretization. The former is adopted for the variables δ_l, δ_s, $\mathbf{U}_l$ and $\mathbf{U}_s$, defined at the grid cell centres, the latter for the bed elevation z_B, with the control volumes constructed around the mesh nodes by the median-dual partition (Barth & Jespersen 1989; Delis *et al.* 2011). The numerical fluxes in the CCFV discretization of Equations (1)–(4) are calculated through the first-order Harten–Lax–Van Leer (HLL) scheme (Harten *et al.* 1983), with second-order reconstruction of the free-surface elevation for subcritical flows, and an appropriate treatment of the bed slope source term is included (Greco *et al.* 2008).

RESULTS AND DISCUSSION

The model discussed in the previous section has been applied to the numerical simulation of the problem sketched in Figure 1. In the first simulation, the floodplain is assumed to be non-erodible, while in the second series of simulations it is assumed constituted by loose sediments. Two scenarios have been considered by changing the sediment diameter from 5×10^{-4} m (denoted as Test 1), representative of fine sand, to 5×10^{-3} m (denoted as Test 2), which is typical of very coarse sand. In the simulations, the following values of the parameters are assumed: $\rho_s = 2{,}650$ kg/m^3, $\mu_d = 25°$, $\mu_s = 38°$, $K_{KMPM} = 8$ and $c_1 = 0.25$. To isolate the effect of bed mobility, in both erodible and non-erodible tests, the same value of the dimensionless Chezy coefficient, $C_{Ch} = 12$, is adopted. A computational mesh with $\Delta x = \Delta y = 5 \times 10^{-3}$ m used, along with $\Delta t = 1/1024$ s. Based on the simulated flow fields, the impact force is evaluated by numerically computing the following integral (Di Cristo *et al.* 2018b):

$$\begin{aligned} \mathbf{F} = \rho_l \int_\sigma \left(\delta_l \mathbf{U}_l U_{l,n} + g\frac{h^2}{2}\hat{\mathbf{n}} \right) d\sigma \\ + \rho_s \int_\sigma \left(\delta_s \mathbf{U}_s U_{s,n} + \frac{r}{r+1}\frac{g\delta_s^2}{2C_s}\hat{\mathbf{n}} \right) d\sigma \end{aligned} \tag{14}$$

where σ denotes the boundary of the obstacle and $\hat{\mathbf{n}}$ is the corresponding normal unit vector. The values of the flow variables in the cells adjacent to the obstacle are used.

Figure 2 shows the time history of the impact force F on the obstacle for the fixed and mobile bed cases, along with the simulation results from the shallow-water model of Aureli *et al.* (2015). As far as the non-erodible case is

Downloaded from https://iwaponline.com/jh/article-pdf/doi/10.2166/hydro.2019.014/569419/jh2019014.pdf
by guest

Corrected Proof

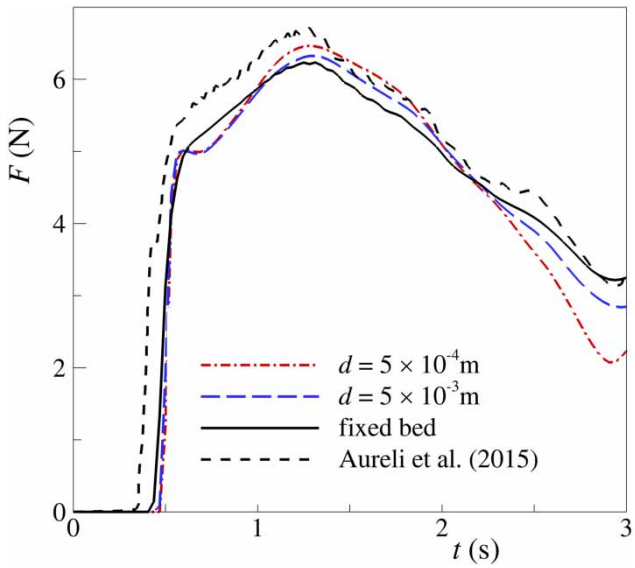

Figure 2 | Time history of the impact forces over the downstream obstacle for fixed and mobile bed cases.

concerned, the results fairly agree with those of Aureli *et al.* (2015), even though the force values predicted herein are slightly smaller. This is attributed to the different resistance formula employed in Aureli *et al.* (2015), i.e., Manning instead of Chezy, and to the value of the dimensionless Chezy coefficient used in the present calculations. Indeed, as shown in Di Cristo *et al.* (2019), increasing the C_{Ch} value up to 25, the agreement between the results of two simulations is strongly improved. After the impact of the wave on the obstacle ($t \sim 0.5$ s), an abrupt increase of the force is observed, which reaches its maximum value ($F \sim 6$ N) at $t \sim 1.25$ s, and then it quasi-monotonically decreases, reaching half of the peak value at $t \sim 3.0$ s, when the flood wave completely surrounds the obstacle. Bottom mobility only marginally influences the load dynamics on the obstacle, especially in the first instants. The time at which the impact and the peak force occur, along with the peak force, only slightly depends on the sediment composing the mobile bottom.

A preliminary discussion of the local characteristics of the flow field has been presented in Di Cristo *et al.* (2018a). That discussion focused mainly on the results at $t = 3$ s, at which the flood wave reattaches behind the obstacle. This time is representative of the final part of the investigated process, as the bottom geometry changes slightly going on. In the previous paper, it has been noted that the fine sediment promotes the reattachment of the flow and a reduced flow height in front of the obstacle is observed, which is consistent with the lower values of the impact force (Figure 2). As far as the bottom topographies are concerned, the case with the fine sediment is characterized by a more pronounced scour hole just downstream the original dam position and at the upstream corners of the obstacle (with depths of about 0.07 m). Finally, it is observed that the interaction with the coarser sediment produces a reduction of the momentum in the region close to the original dam.

In what follows a more detailed analysis is provided, which is mainly focused on the near- and mid-field phase of the evolution of the process ($t \leq 2.0$ s). Namely, the free- and bed-surface elevation of the solid-phase volume (for the unit bottom surface) transported as bed load (δ_s) for the two cases $d = 5 \times 10^{-4}$ m (denoted as Test 1) and $d = 5 \times 10^{-3}$ m (denoted as Test 2) are discussed in Figures 3–7 for different instants. Moreover, for the sake of comparison, the free-surface elevation of the fixed bed (denoted as Test 0) is also shown.

At $t = 0.25$ s, Figure 3(b) and 3(c) indicate that the free-surface elevation for Test 2 and Test 0 shows only marginal differences. On the other hand, in the $d = 5 \times 10^{-4}$ m case (Figure 3(a)), the shape of the wave is characterized by a more pronounced diffusion in the transversal direction. Namely, the longitudinal distance reached by the wave front does not substantially differ from the other two tests, whereas the width of the wave body in the transversal direction is sensibly larger. Indeed, while in Test 1 the bed load is already appreciable, in the $d = 5 \times 10^{-3}$ m case, it is only perceivable (Figure 3(d) and 3(e)). At the same instant, the erosion process is taking place in the $d = 5 \times 10^{-4}$ m case while it is negligible in Test 2 (Figure 3(f) and 3(g)).

For all the tests, the time $t = 0.5$ s is very close to the moment in which the wave impacts against the obstacle (see Figure 2). Soon after, the wave is deflected and splits into two symmetrical bodies flowing laterally to the obstacle (Figure 4(a)–4(c)). The comparison among Figure 4(a)–4(c) indicates that the fixed-bed case is characterized by the highest value of the celerity propagation, as suggested by the time evolution of the impact force shown in Figure 2.

Downloaded from https://iwaponline.com/jh/article-pdf/doi/10.2166/hydro.2019.014/569419/jh2019014.pdf
by guest

Corrected Proof

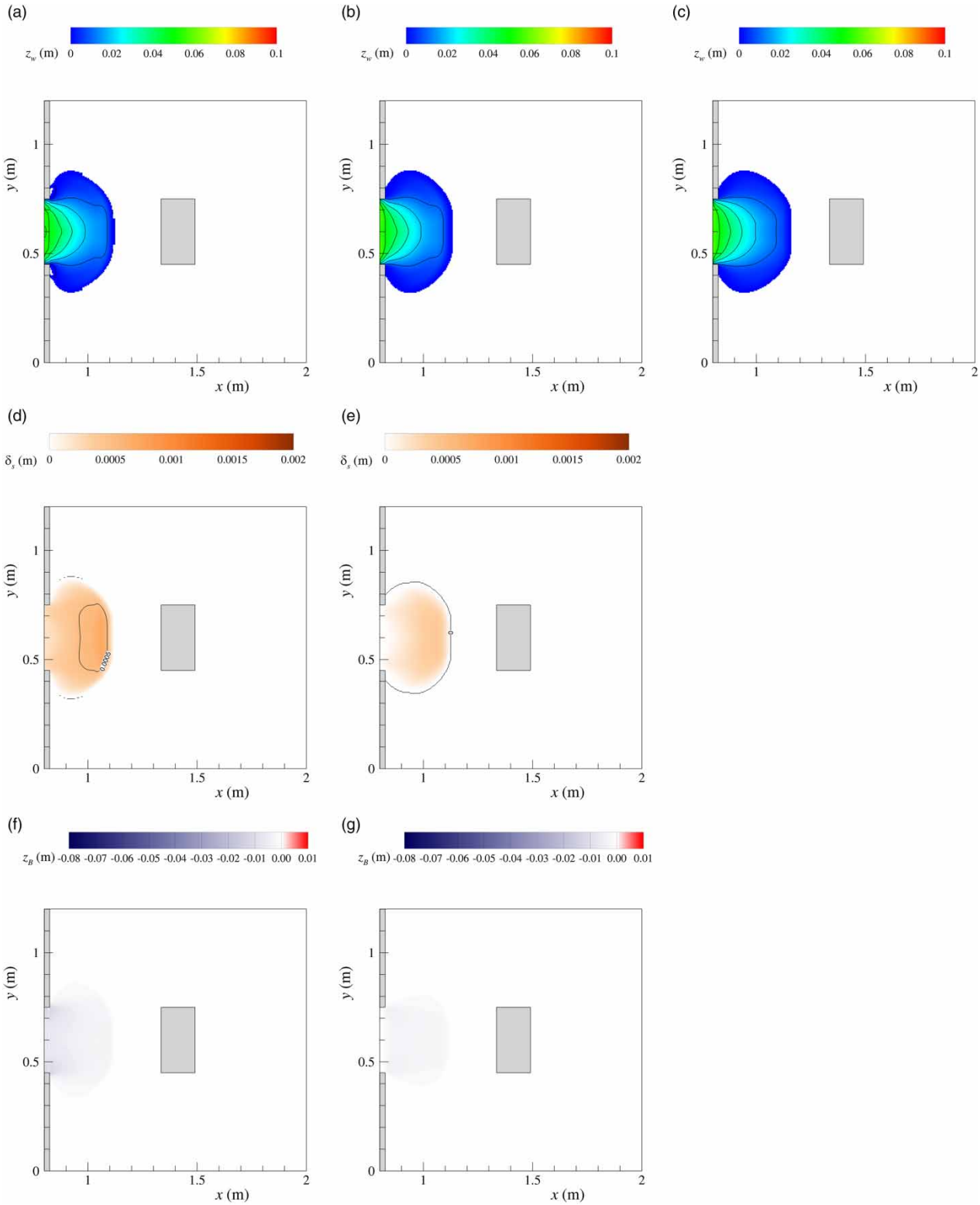

Figure 3 | Results at $t = 0.25$ s. Free-surface elevation for $d = 5 \times 10^{-4}$ m (a), $d = 5 \times 10^{-3}$ m (b) and fixed bed (c). Bedload solid-phase volume (for the unit bottom surface) for $d = 5 \times 10^{-4}$ m (d) and $d = 5 \times 10^{-3}$ m (e). Bottom erosion/deposition for $d = 5 \times 10^{-4}$ m (f) and $d = 5 \times 10^{-3}$ m (g).

Downloaded from https://iwaponline.com/jh/article-pdf/doi/10.2166/hydro.2019.014/569419/jh2019014.pdf
by guest

Corrected Proof

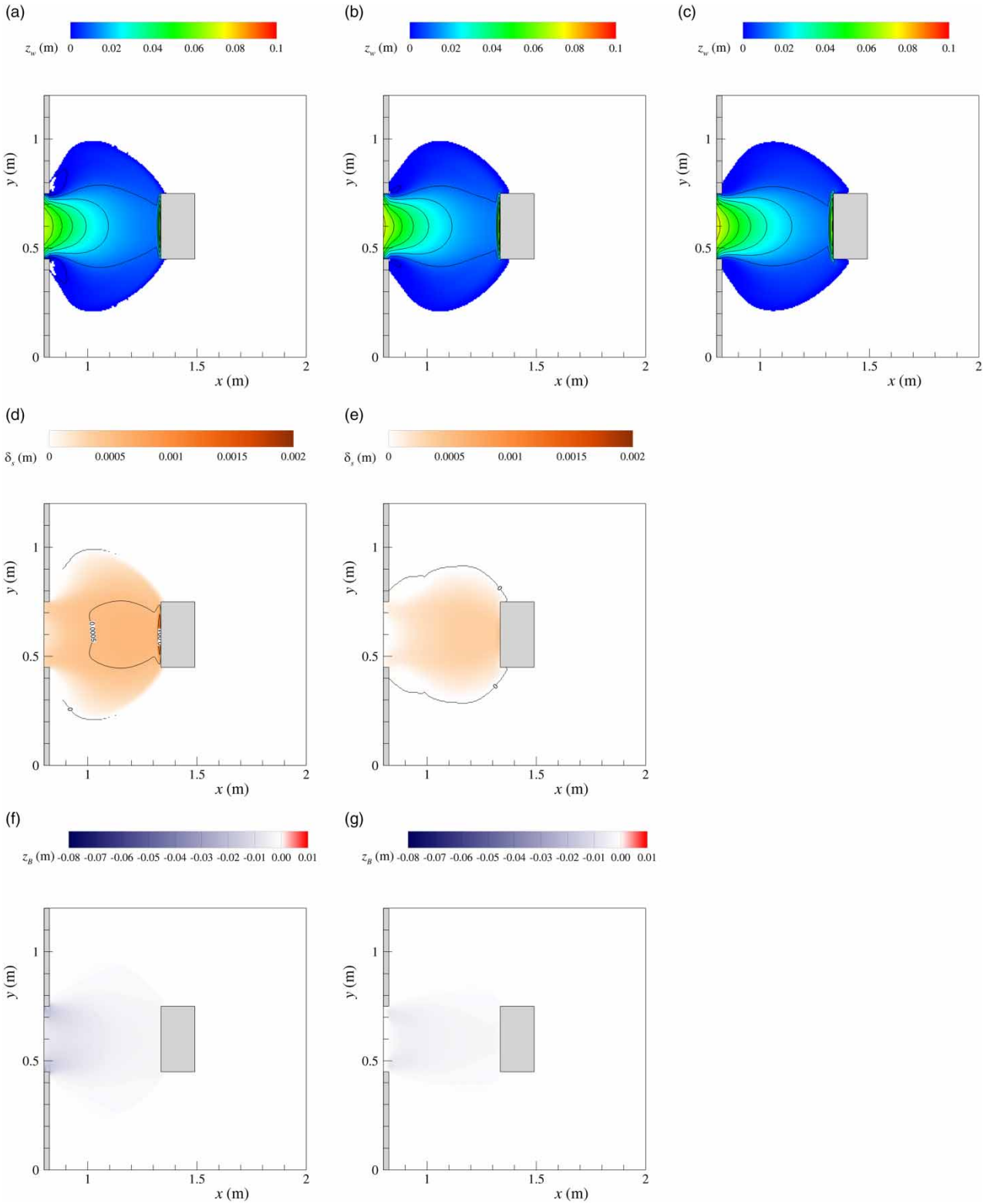

Figure 4 | Results at $t =$ 0.5 s. Free-surface elevation for $d = 5 \times 10^{-4}$ m (a), $d = 5 \times 10^{-3}$ m (b) and fixed bed (c). Bedload solid-phase volume (for the unit bottom surface) for $d = 5 \times 10^{-4}$ m (d) and $d = 5 \times 10^{-3}$ m (e). Bottom erosion/deposition for $d = 5 \times 10^{-4}$ m (f) and $d = 5 \times 10^{-3}$ m (g).

Downloaded from https://iwaponline.com/jh/article-pdf/doi/10.2166/hydro.2019.014/569419/jh2019014.pdf
by guest

Corrected Proof

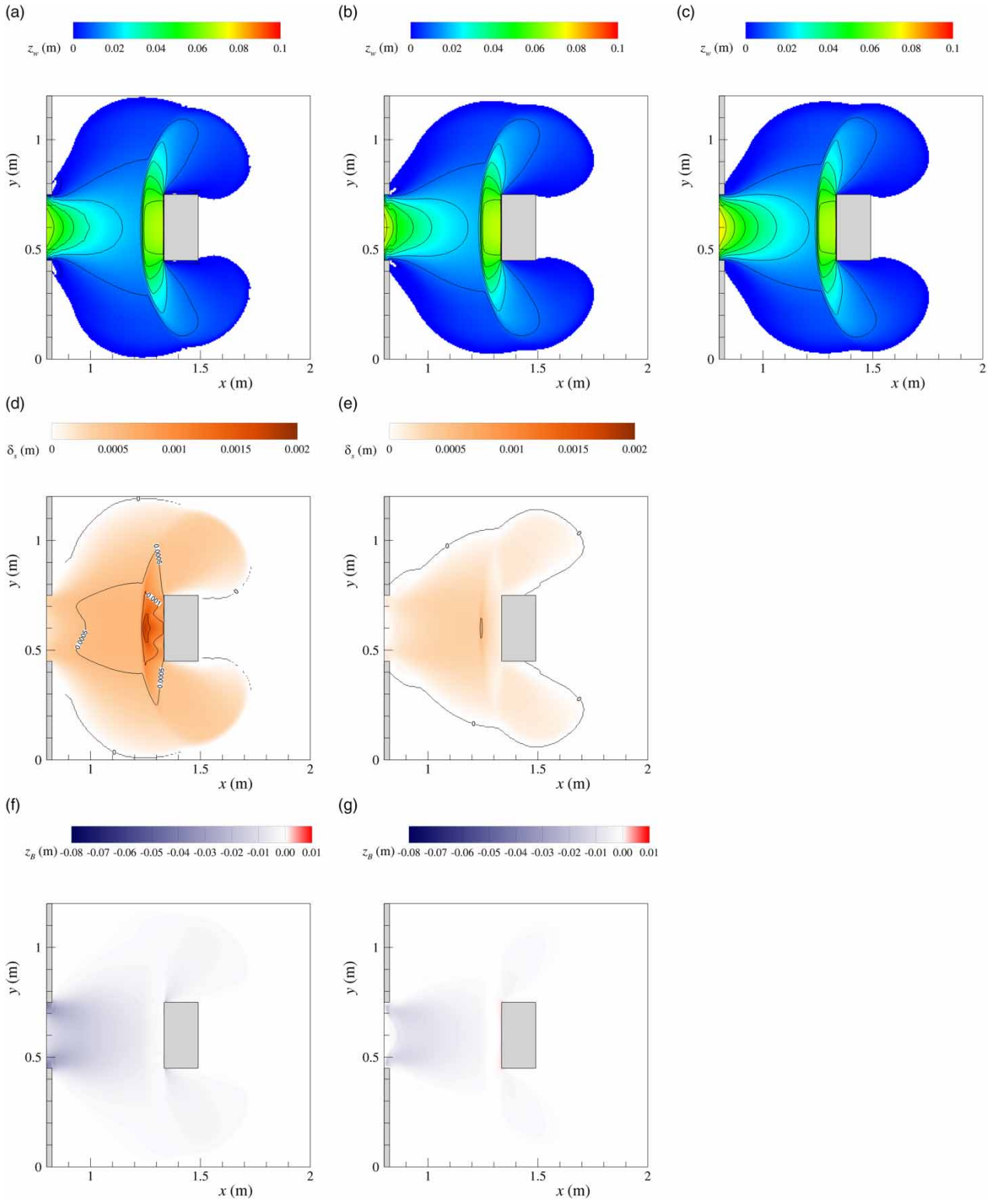

Figure 5 | Results at $t =$ 1.0 s. Free-surface elevation for $d = 5 \times 10^{-4}$ m (a), $d = 5 \times 10^{-3}$ m (b) and fixed bed (c). Bedload solid-phase volume (for the unit bottom surface) for $d = 5 \times 10^{-4}$ m (d) and $d = 5 \times 10^{-3}$ m (e). Bottom erosion/deposition for $d = 5 \times 10^{-4}$ m (f) and $d = 5 \times 10^{-3}$ m (g).

Downloaded from https://iwaponline.com/jh/article-pdf/doi/10.2166/hydro.2019.014/569419/jh2019014.pdf
by guest

Corrected Proof

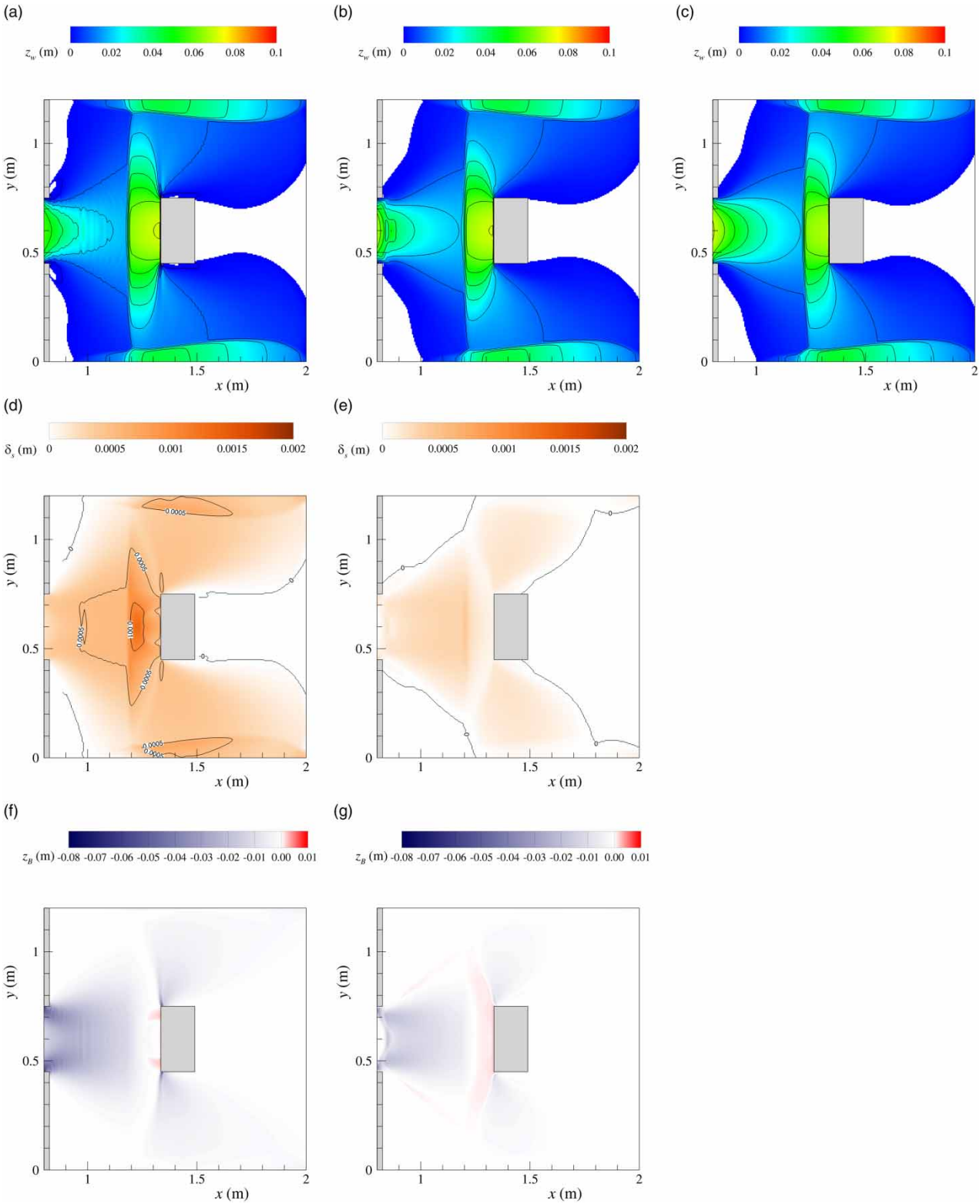

Figure 6 | Results at $t =$ 1.5 s. Free-surface elevation for $d = 5 \times 10^{-4}$ m (a), $d = 5 \times 10^{-3}$ m (b) and fixed bed (c). Bedload solid-phase volume (for the unit bottom surface) for $d = 5 \times 10^{-4}$ m (d) and $d = 5 \times 10^{-3}$ m (e). Bottom erosion/deposition for $d = 5 \times 10^{-4}$ m (f) and $d = 5 \times 10^{-3}$ m (g). Please refer to the online version of this paper to see this figure in colour: http://dx.doi.org/10.2166/hydro.2019.014.

Downloaded from https://iwaponline.com/jh/article-pdf/doi/10.2166/hydro.2019.014/569419/jh2019014.pdf
by guest

Corrected Proof

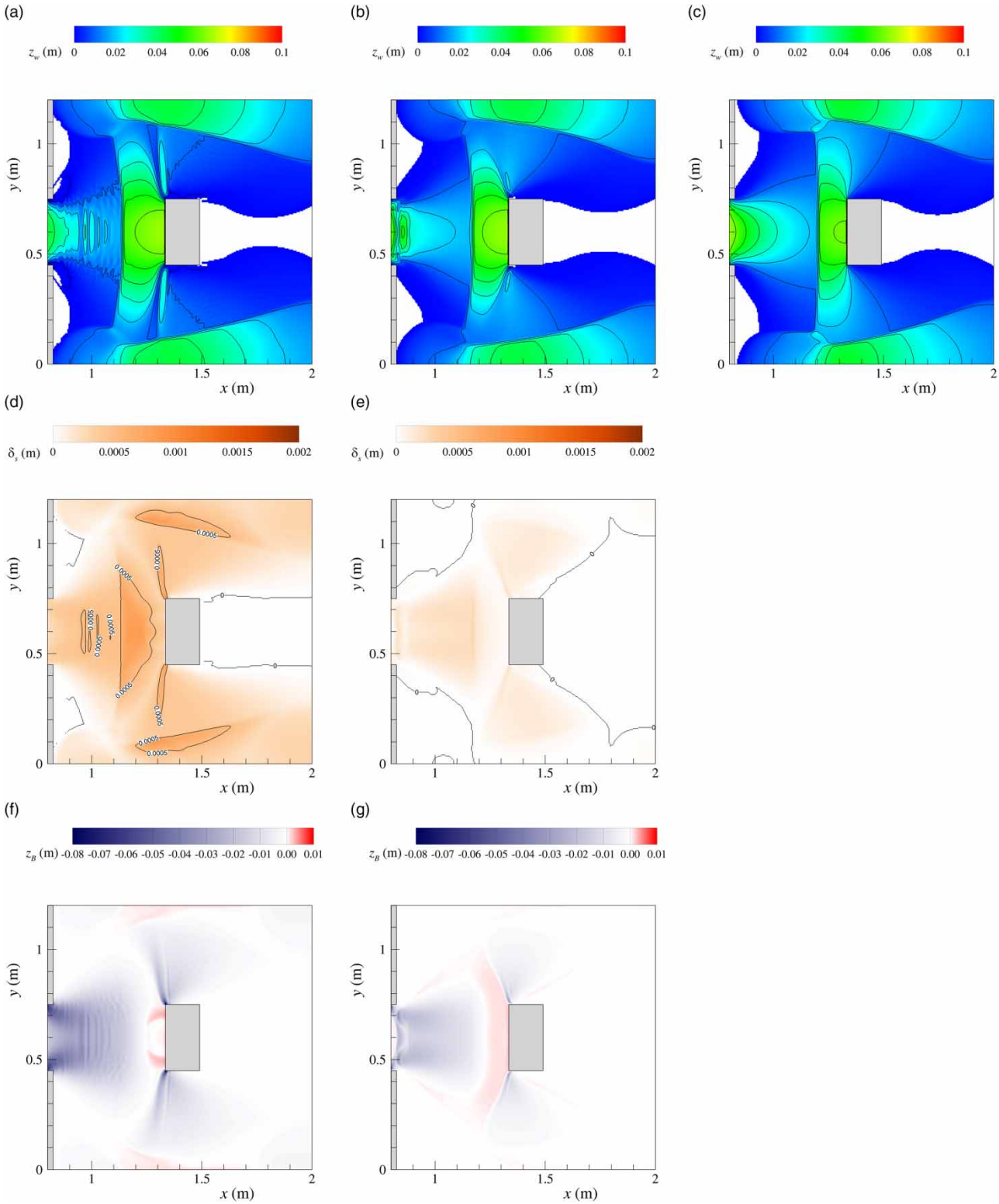

Figure 7 | Results at $t = 2.0$ s. Free-surface elevation for $d = 5 \times 10^{-4}$ m (a), $d = 5 \times 10^{-3}$ m (b) and fixed bed (c). Bedload solid-phase volume (for the unit bottom surface) for $d = 5 \times 10^{-4}$ m (d) and $d = 5 \times 10^{-3}$ m (e). Bottom erosion/deposition for $d = 5 \times 10^{-4}$ m (f) and $d = 5 \times 10^{-3}$ m (g).

Downloaded from https://iwaponline.com/jh/article-pdf/doi/10.2166/hydro.2019.014/569419/jh2019014.pdf
by guest

Corrected Proof

Interestingly, the presence of erodible bottom appears to slow down the celerity of the wave, even though this effect is marginally influenced by the sand diameter value. Globally, independently of the sand diameter, the presence of erodible bed only marginally influences the hydrodynamics of the wave at this instant (see Figure 4(a)–4(c)). However, the main peculiarity of the erodible bed cases at this instant is the presence of a recirculation zone in the region very close to the gate. This flow feature is particularly evident in Test 1 (Figure 4(a)), whereas it is not found in Test 0. The δ_s maps (Figure 4(d) and 4(e)) put in evidence that, owing to the large diameter of the sand, in Test 2, the bedload transport occurs mainly in the centre of the wave, where the high velocity values are able to entrain sediments from the bottom (Figure 4(e)). In contrast, in the $d = 5 \times 10^{-4}$ m case (Figure 4(a)), the δ_s footprint strongly resembles one of the liquid phases and therefore almost everywhere the fluid flow is able to entrain sediment from the erodible bottom inducing the bedload movement. The differences in the erosion/deposition process between Tests 1 and 2 are clearly shown in Figure 4(f) and 4(g). The high velocity values very close to the gate produce an intense erosion process, which is more evident for the simulation with fine sand (Figure 4(f)) rather than in the $d = 5 \times 10^{-3}$ m case (Figure 4(g)).

At $t = 1.0$ s (Figure 5), in all tests, the wave surrounds the obstacle, laterally deflecting and overcoming it. However, the deflected wave has not reached the lateral walls yet. Moreover, created by the reflection of the impacting wave against the obstacle, a discontinuous front just upstream the obstacle is visible in all cases. While in Test 2 the shape of the wave still strongly resembles one of the fixed-bed simulation (Figure 5(b) and 5(c)), the small value of sand diameter in Test 1 causes a transversal diffusion stronger than in Test 0. In the $d = 5 \times 10^{-4}$ m case, the intense bedload, witnessed by the high δ_s values just upstream of the obstacle, suggests that a strong momentum transfer from the liquid phase towards the solid one is occurring (Figure 5(d)). The erosion process, which is particularly violent in the zone just downstream of the gate, induces a consistent reduction of the surface bed elevation (Figure 5(f)). Moreover, starting from the upstream edges of the obstacle, two thin eroded limbs are clearly appreciable. In Test 2, the bed load activity is weaker than in Test 1, and it takes place in a smaller portion of the channel (Figure 5(e) and 5(g)).

At $t = 1.5$ s in all tests (Figure 6(a)–6(c)), the impact of the wave with the lateral walls has taken place because of the lateral deflection, and moreover, two additional discontinuous wave fronts are generated symmetrically with respect to the obstacle. The wave reaches the flume outlet and leaves a large dry region behind the obstacle. The comparison between Figure 6(a) and 6(c) demonstrates that the bed erodibility promotes the lateral wave distortion. The movement of the solid phase is seen to strictly follow the water movement in the $d = 5 \times 10^{-4}$ m case, although, due to the interaction of the two-phase current with the solid walls (obstacle and lateral walls), three localized islands with high values of δ_s have been created (Figure 6(d)). In Test 2, the solid transport is less vigorous than in Test 1, and it occurs only dowstream of the obstacle (Figure 6(e)). The intense bedload leads in Test 1 contributes to a solid deposition in a very concentrated zone just upstream of the obstacle (Figure 6(f), red colour). In contrast, in the $d = 5 \times 10^{-3}$ m case, the deposition process occurs, still upstream of the obstacle, but in a larger part of the channel than in Test 1 (Figure 6(g)).

Figure 7 shows that, independently of the bed erodibility, at $t = 2.0$ s the discontinuous fronts created by the interaction of the two currents with the lateral walls propagate symmetrically towards the centre of the channel, significantly reducing the extension of the dry zone present in the back of the obstacle. Such a modification is particularly evident in the $d = 5 \times 10^{-4}$ m case (Figure 7(a)). In Test 1, the erodibility of the bed determines the presence of superficial waves characterized by small values of wavelength which are seen to be associated with bed forms (see Figure 7(a), 7(d) and 7(f)). Similar bed forms have been frequently found in analogous geomorphic transients (e.g. Spinewine & Zech 2010) and, as it has been theoretically shown, their formation may be described even by a shallow-water approach, provided that a dynamic description for the sediment transport is considered (Di Cristo *et al.* 2006; Vesipa *et al.* 2012; Greco *et al.* 2018). Finally, the zones close to the upstream edge of the obstacle in which a deposition started at $t = 1.0$ s increase their extension and, moreover, a deposition process occurs symmetrically close to the lateral walls. In Test 2, the presence of bed

Downloaded from https://iwaponline.com/jh/article-pdf/doi/10.2166/hydro.2019.014/569419/jh2019014.pdf
by guest

Corrected Proof

forms is not detected, and only a deposition process is found upstream of the obstacle but in a smoother way than in Test 1. The geometry of this depositional pattern is elongated in the transversal for an extension approximately three times the obstacle width. No appreciable deposition is detected alongside the lateral walls.

The analysis of the present process with a two-phase morphodynamical model provides the opportunity to discuss the effects of the grain size on the dynamics of the solid phase during the impact against the obstacle. To this aim, Figure 8 compares the velocity vector plots referring to the two Test Cases 1 and 2, representing the velocity field of both the liquid and the solid phases at $t = 1.0$ s. At this time, the wave overcomes the obstacle, and the fluid/sediment mixture is deflected in the lateral direction.

The results obtained with the fine sand (Figure 8(a)) show that the velocity vectors of the solid phase have a smaller magnitude of the liquid-phase ones, but they present nearly the same direction. The magnitude of maximum difference between the velocities, i.e. the maximum of the module of the difference between the liquid and the solid velocities, is 0.44 m/s. In contrast, the coarse sand (Figure 8(b)) is characterized by a much more pronounced resistance to adapt to the change in the flow direction induced by the impact against the obstacle, and a sensible disalignment of the velocity vectors of the two phases is detected in the region close to the obstacle corner. In this case, the magnitude of maximum difference between the velocity of the solid and liquid phases is 0.64 m/s. This result and the comparison between Figure 8(a) and 8(b) demonstrate that the hypothesis of collinearity of the motion direction of the two phases, which is assumed in the single phase and the mixture models, may fail in the presence of coarse sand, whereas it is reasonably satisfied if the sediment is sufficiently fine.

CONCLUSIONS

In the present paper, a numerical study of the impact of a dam-break wave propagating over an erodible floodplain against a rigid obstacle has been discussed. The investigated condition has been inspired by a laboratory experiment recently reported in the literature with a non-erodible bed. To cope with the features of the complex morphodynamics characterizing the present test case, a recent shallow-water two-phase model, numerically integrated with a proper method, has been adopted. Results have been analysed in terms of impact force on the obstacle, flow field and bottom deformation. The effect of the bottom erodibility has been discussed by comparing with the corresponding fixed-bed condition. Moreover, the effect of the diameter of the sediment constituting the loose bed on the two-phase

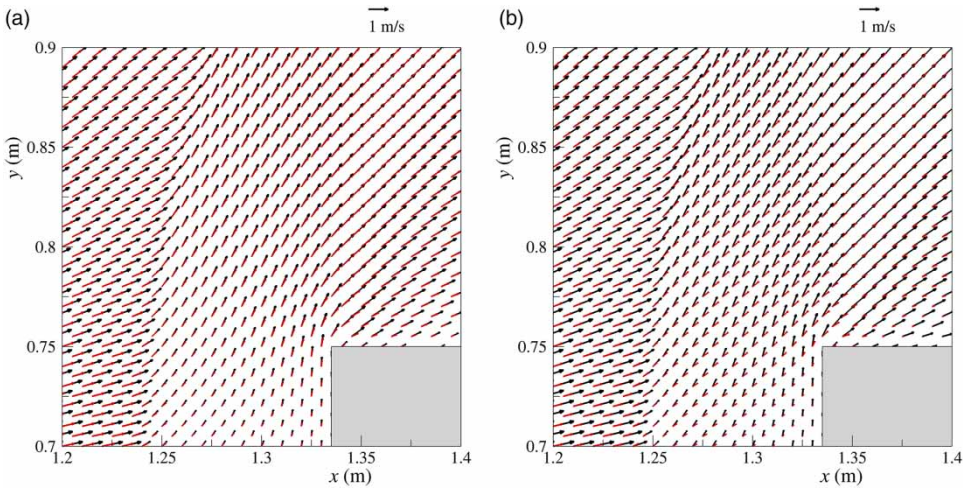

Figure 8 | Velocity vector plots for $d = 5 \times 10^{-4}$ m (a) and $d = 5 \times 10^{-3}$ m (b). Black (red) arrows refer to liquid (solid)-phase velocities. Vector density has been reduced to improve readability. Please refer to the online version of this paper to see this figure in colour: http://dx.doi.org/10.2166/hydro.2019.014.

Downloaded from https://iwaponline.com/jh/article-pdf/doi/10.2166/hydro.2019.014/569419/jh2019014.pdf
by guest

Corrected Proof

flow field and on the bottom evolution has been discussed for fine and coarse sand.

Bottom mobility has been found to affect the shape of the wave starting from the very beginning of the geomorphic transient, influencing the propagation of the wet-dry front in the transversal direction, especially for fine sand. As far as the evolution of the erodible bottom is concerned, fine sand has been found to determine more pronounced scour at the original dam location and at the upstream corners of the impacted obstacles compared to the case with coarse sand. On the other hand, the coarse sediment induces the appearance of a larger deposit area immediately upstream of the obstacle, elongated in the transversal direction with a width of about three times the obstacle. Additionally, the analysis of the flow field of solid and liquid phases has shown that under similar circumstances, the hypothesis of collinearity of the motion direction of solid and liquid phases, adopted in the single phase and mixture models, may fail in the presence of coarse sand.

ACKNOWLEDGEMENTS

The work described in the present paper was realized in the framework of the project MISALVA and financed by the Italian Minister of the Environment, Land Protection and Sea (CUP H36C18000970005).

REFERENCES

Aureli, F., Dazzi, S., Maranzoni, A., Mignosa, P. & Vacondio, R. 2015 Experimental and numerical evaluation of the force due to the impact of a dam-break wave on a structure. *Adv. Wat. Res.* **76**, 29–42.

Barth, T. J. & Jespersen, D. C. 1989 *The design and application of upwind schemes on unstructured meshes*. AIAA Paper 89-0366.

Bukreev, V. I. 2009 Force action of discontinuous waves on a vertical wall. *J. Appl. Mech. Tech. Phys.* **50** (2), 278–283.

Canelli, L., Ferrero, A. M., Migliazza, M. & Segalini, A. 2012 Debris flow risk mitigation by means of rigid and flexible barriers – experimental tests and impact analysis. *Nat. Hazard Earth Syst. Sci.* **12**, 1693–1699. doi:10.5194/nhess-12-1693-2012.

Capart, H. & Young, D. 2002 Two-layer shallow water computations of torrential geomorphic flows. In: *Proc. of River Flow 2002*. Swets & Zeitlinger, Lisse, Netherlands, pp. 1003–1012.

Chen, H. Y., Xu, W. L., Deng, J., Xue, Y. & Li, J. 2014 Experimental investigation of pressure load exerted on a downstream dam by dam-break flow. *J. Hydr. Eng.* **140** (2), 199–207. doi:1943-7900.0000743.

Chiou, M. C., Wang, Y. & Hutter, K. 2005 Influence of obstacles on rapid granular flows. *Acta. Mech.* **175**, 195–122. doi:10.1007/s00707-004-0208-9.

Cui, P. & Gray, J. M. N. T. 2013 Gravity driven granular free-surface flow around a circular cylinder. *J. Fluid. Mech.* **720**, 314–337.

Delis, A. I., Nikolos, I. K. & Kazolea, M. 2011 An unstructured node-centered finite volume scheme for shallow water flows with wet/dry fronts over complex topography. *Arch. Comput. Meth. Eng.* **18**, 57–118.

Dewals, B., Rulot, F., Erpicum, S., Archambeau, P. & Pirotton, M. 2011 *Advanced Topics in Sediment Transport Modelling: Non-Alluvial Beds and Hyperconcentrated Flows, Sediment Transport*. Available from: http://www.intechopen.com/books/sediment-transport/advanced-topics-in-sediment-transport-modelling-non-alluvial-beds-and-hyperconcentrated-flows.

Di Cristo, C., Iervolino, M. & Vacca, A. 2006 Linear stability analysis of a 1-D model with dynamical description of bed load transport. *J. Hydr. Res.* **44**, 480–487. doi:10.1080/00221686.2006.9521699.

Di Cristo, C., Greco, M., Iervolino, M., Leopardi, A. & Vacca, A. 2016 Two-dimensional two-phase depth-integrated model for transients over mobile bed. *J. Hydr. Eng.* **142** (2), 04015043.

Di Cristo, C., Greco, M., Iervolino, M. & Vacca, A. 2018a Numerical simulation of a dam-break wave propagating over an erodible floodplain in presence of a structure. In: *HIC 2018 EPiC Series in Engineering* (G. La Loggia, G. Freni, V. Puleo & M. De Marchis, eds), 3, pp. 564–571.

Di Cristo, C., Evangelista, S., Greco, M., Iervolino, M., Leopardi, A. & Vacca, A. 2018b Dam-break waves over an erodible embankment: experiments and simulations. *J. Hydr. Res.* **56** (2), 196–210. doi:10.1080/00221686.2017.1313322.

Di Cristo, C., Greco, M., Iervolino, M. & Vacca, A. 2019 Numerical simulation of mud-flows impacting structures. *J. Mount. Sc.* **16** (2), 364–382. doi:10.1007/s11629-018-5279-5.

El Kadi Abderrezzak, K., Paquier, A. & Mignot, E. 2009 Modelling flash flood propagation in urban areas using a two-dimensional numerical model. *Nat. Haz.* **50**, 433–460.

Faug, T. 2015 Depth-average analytical solution for free-surface granular flow impacting rigid walls down inclines. *Phys. Rev. E* **92**, 062310. doi:10.1103/PhysRevE.9292.062310.

Gao, L., Zhang, L. M. & Chen, H. X. 2017 Two dimensional simulation of debris flow impact pressure on buildings. *Eng. Geol.* **226**, 236–244. doi:10.1016/j.enggeo.2017.06.012.

Greco, M., Iervolino, M. & Leopardi, A. 2008 Discussion of 'divergence form for bed slope source term in shallow water equations' by Alessandro Valiani and Lorenzo Begnudelli. *J. Hydr. Eng.* **134** (5), 676–678. doi:10.1061/(ASCE)0733-9429(2008)134:5(676).

Downloaded from https://iwaponline.com/jh/article-pdf/doi/10.2166/hydro.2019.014/569419/jh2019014.pdf
by guest

Corrected Proof

Greco, M., Iervolino, M., Leopardi, A. & Vacca, A. 2012 A two-phase model for fast geomorphic shallow flows. *Int. J. Sed. Res.* **27** (4), 409–420.

Greco, M., Iervolino, M. & Vacca, A. 2018 Analysis of bedform instability with 1-D two-phase morphodynamical models. *Adv. Water Resour.* **120**, 50–64. doi:10.1016/j.advwatres.2017.07.002.

Harten, A., Lax, P. D. & van Leer, B. 1983 On upstream differencing and Godunov-type schemes for hyperbolic conservation laws. *SIAM Rev.* **25** (1), 35–61.

Hoerling, M. P., Hurrell, J. W. & Xu, T. 2001 Tropical origin for recent North Atlantic climate change. *Science* **292**, 90–92.

Hung, O., Morgan, G. C. & Kelerhals, R. 1984 Quantitative analysis of debris torrent hazard for design of remedial measures. *Can. Geotech. J.* **21**, 663–677.

Kattel, P., Kafle, J., Fischer, J. T., Mergili, M., Tuladhar, B. M. & Pudasaini, S. P. 2018 Interaction of two-phase debris with obstacles. *Eng. Geol.* **242**, 197–217. doi:10.1016/j.enggeo.2018.05.023.

Kelman, I. & Spence, R. 2004 An overview of flood actions on buildings. *Eng. Geol.* **73** (2004), 297–309.

Li, J., Cao, Z., Pender, G. & Liu, Q. 2013 A double layer-averaged model for dam-break flows over mobile bed. *J. Hydr. Res.* **51** (5), 518–534.

Lobovsky, L., Botia-Vera, E., Castellana, F., Mas-Soler, J. & Souto-Iglesias, A. 2014 Experimental investigation of dynamic pressure loads during dam break. *J. Fluid Struct.* **48** (2014), 407–434.

Palumbo, A., Soares-Frazão, S., Goutiere, L., Pianese, D. & Zech, Y. 2008 Dam-break flow on mobile bed in a channel with a sudden enlargement. *Proc. River Flow* **2008**, 645–654.

Pontillo, M., Schmocker, L., Greco, M. & Hager, W. H. 2010 1D numerical evaluation of dike erosion due to overtopping. *J. Hydr. Res.* **48** (5), 573–582.

Pudasaini, S. P. 2012 A general two-phase debris flow model. *J. Geophys. Res.* **117**, F03010. doi:10.1029/2011JF002186.

Richardson, J. F. & Zaki, W. N. 1954 Sedimentation and fluidisation: part 1. *Trans. Inst. Chem. Eng.* **32**, 35–53.

Rosatti, G. & Begnudelli, L. 2013 A closure-independent Generalized Roe solver for free-surface, two-phase flows over mobile bed. *J. Comp. Phys.* **255**, 362–383.

Savary, C. & Zech, Y. 2007 Boundary conditions in a two-layer geomorphological model: application to a hydraulic jump over a mobile bed. *J. Hydr. Res.* **45** (3), 316–332.

Scheidl, C., Chiari, M., Kaitna, R., Mullegger, M., Krawtschuk, A., Zimmermann, T. & Proske, D. 2013 Analysing debris-flow impact model, based on small scale modelling approach. *Surv. Geophys.* **34** (1), 121–140.

Shige-eda, M. & Akiyama, J. 2003 Numerical and experimental study on two-dimensional flood flows with and without structures. *J. Hydr. Eng.* **129** (10), 817–821.

Soares-Frazão, S. & Zech, Y. 2007 Experimental study of dam-break flow against an isolated obstacle. *J. Hydr. Res.* **45** (Supp1), 27–36. doi:10.1080/00221686.2007.9521830.

Soares-Frazao, S. & Zech, Y. 2008 Dam-break flow through an idealised city. *J. Hydr. Res.* **46** (5), 648–658.

Soares-Frazão, S., Canelas, R., Cao, Z., Cea, L., Chaudhry, H. M., Die Moran, A., El Kadi, K., Ferreira, R., Fraga Cadórniga, I., Gonzalez-Ramirez, N., Greco, M., Huang, W., Imran, J., Le Coz, J., Marsooli, R., Paquier, A., Pender, G., Pontillo, M., Puertas, J., Spinewine, B., Swartenbroekx, C., Tsubaki, R., Villaret, C., Wu, W., Yue, Z. & Zech, Y. 2012 Dam-break flows over mobile beds: experiments and benchmark tests for numerical models. *J. Hydr. Res.* **50** (4), 364–375.

Spinewine, B. & Zech, Y. 2010 Small-scale laboratory dam-break waves on movable beds. *J. Hydr. Res.* **45** (Supp1), 73–86.

Swartenbroekx, C., Zech, Y. & Soares Frazão, S. 2013 Two-dimensional two-layer shallow water model for dam break flows with significant bed load transport. *Int. J. Num. Meth. Fluids* **73** (5), 477–508.

Tai, Y. C., Gray, J. M. N. & Hutter, C. 2001 Flow dense avalanches past obstructions. *Ann. Glaciol.* **32**, 281–284.

Teufelsbauer, H., Wang, Y., Chou, C. & Wu, W. 2009 Flow obstacle-interaction in rapid granular avalanches: DEM simulation and comparison with experiments. *Granular. Matter.* **11** (4), 209–220. 10.1007/s10035-009-0142-6.

Thieken, A. H., Muller, M., Kreibich, H. & Merz, B. 2005 Food damage and influencing factors: new insights from the August 2002 flood in Germany. *Water Resour. Res.* **41** (12), W12430.

Van Rijn, L. C. 1984 Sediment pick-up functions. *J. Hydr. Eng.* **110** (10), 1494–1502.

Vesipa, R., Camporeale, C. & Ridolfi, L. 2012 A shallow-water theory of river bedforms in supercritical conditions. *Phys. Fluids.* **24**, 094104. doi:10.1063/1.4753943.

Wang, J. S., Ni, H. G. & He, Y. S. 2000 Finite-difference TVD scheme for computation of dam break problems. *J. Hydr. Eng.* **126** (4), 253–262. doi:10.1061/(ASCE)0773-9429.

Wu, W. & Wang, S. S.-Y. 2007 One dimensional modeling of dam break flow over movable beds. *J. Hydr. Eng.* **133** (1), 48–58.

First received 14 January 2019; accepted in revised form 18 April 2019. Available online 21 May 2019

Downloaded from https://iwaponline.com/jh/article-pdf/doi/10.2166/hydro.2019.014/569419/jh2019014.pdf
by guest